The Dependence of TOA Reflectance Anisotropy on Cloud Properties Inferred from ScaRaB Satellite Data

FU-LUNG CHANG, ZHANQING LI, AND ALEXANDER P. TRISHCHENKO

Canada Centre for Remote Sensing, Ottawa, Ontario, Canada.

ABSTRACT

An angular dependence model (ADM) describes the anisotropy in the reflectance field. ADMs are a key element in determining the top-of-the-atmosphere (TOA) albedos and radiative fluxes. This study utilizes 1-yr satellite data from the Scanner for Radiation Budget (ScaRaB) for overcast scenes to examine the variation of ADMs with cloud properties. Using ScaRaB shortwave (SW) overcast radiance measurements, an SW mean overcast ADM, similar to the Earth Radiation Budget Experiment (ERBE) ADM, was generated. Differences between the ScaRaB and ERBE overcast ADMs lead to biases of ~0.01–0.04 in mean albedos inferred from specific angular bins. The largest biases are in the backward scattering direction. Overcast ADMs for the visible (VIS) wavelength were also generated using ScaRaB VIS measurements. They are very similar to, but a little smaller at large viewing angles and a little larger at nadir, than the SW overcast ADMs. To evaluate the effect of cloud properties on ADMs, ScaRaB overcast observations were further classified into thin, thick, warm, and cold cloud categories to generate four subsets of ADMs. The resulting ADMs for thin and thick clouds show opposite trends and deviate significantly from the overall mean ADM by more than 10%. Deviations from the mean ADM were also noted for the ADMs developed for warm water clouds and cold ice clouds. These deviations were attributed to the different scattering phase functions of water and ice particles and were compared with results from model simulations. Use of a single mean overcast ADM results in albedo biases of 0.01–0.04, relative to the use of specific ADMs for particular cloud types. The biases reduced to ~0.005 when averaged over all cloud types and viewing geometry.

1. Introduction

The earth's radiation budget (ERB) plays important roles in governing the earth's climate (Wielicki et al. 1995). Accurate knowledge of the ERB is essential to climate studies and modeling (Hartmann et al. 1986; Arking 1991). Several spaceborne programs have been dedicated to monitor the ERB, such as the Earth Radiation Budget Experiment (ERBE) (Barkstrom and Smith 1986) and Clouds and the Earth's Radiant Energy System (CERES) (Wielicki et al. 1996) of the United States, and the Scanner for Radiation Budget (ScaRaB) (Kandel 1994 and 1998) and future Geostationary Earth Radiation Budget (GERB) of Europe. While these programs provide a wealth of information pertinent to ERB and its interaction with clouds, radiative fluxes at the top-of-the-atmosphere (TOA) and their disposition inside the atmosphere and at the surface are still subject to considerable uncertainties (Li et al. 1997a).

Several inversion processes are involved in obtaining broadband irradiances from observed filtered radiance measurements (Smith et al. 1986). The largest uncertainty in deriving instantaneous fluxes originates from the use of an angular dependence model (ADM) to convert radiance into irradiance, while diurnal sampling dictates more the accuracy of daily and monthly mean fluxes (Wielicki et al. 1996). To date, the most complete and widely used ADM was designed for ERBE (Suttles et al. 1988; Manalo-Smith et al. 1998). The ERBE ADMs were defined for 12 scene types, but there is only one ADM for overcast scenes over all types of surfaces. Cloud conditions are better defined in terms of fractional coverage, optical and geometrical thickness, and microphysical properties, but the ERBE ADMs were only differentiated according to four categories of cloud coverage, namely, clear, partly cloudy, mostly cloudy, and overcast (Suttles et al. 1988). More sophisticated ADMs are needed to achieve higher accuracy for clouds with a variety of optical depths and microphysics (Wielicki et al. 1996). Use of inadequate ADMs may hinder understanding of the relation between cloud and radiation. Chang et al. (2000) compared TOA radiative quantities derived from broadband satellite measurements (ERBE) with those computed by a radiative transfer model based on cloud parameters inferred from narrowband Advanced Very High Resolution Radiometer (AVHRR)

Corresponding author address: Zhanqing Li, Canada Centre for Remote Sensing, 588 Booth Street, Ottawa, ON K1A0Y7, Canada. E-mail: li@ccrs.nrcan.gc.ca

data. Good agreements were reached for TOA reflectances, but large discrepancies occurred for TOA albedos for certain cloud optical thickness. The discrepancies were attributed to the use of a single ADM that lacks dependence on cloud optical and microphysical properties (Chang et al. 2000).

ScaRaB has some unique features to tackle ADM-related issues. First, the ScaRaB satellite flew in a non-sun-synchronous orbit, which provided observations at varying geometries between the sun, target, and satellite. Sampling at different angular bins is a prerequisite in developing ADMs. Taking advantage of the extensive angular coverage by ScaRaB, Capderou (1998a) developed a new set of ADMs for desert scenes and compared it with those derived from other satellites. The validity of the Helmholtz reciprocity principle was also examined employing ScaRaB data (Capderou 1998b). Second, ScaRaB carried not only a broadband scanning radiometer like the ERBE radiometer, but also the visible (VIS) and infrared (IR) imagers similar to operational weather satellite sensors. This allowed for a better distinction between scene types and a direct comparison of ADMs for shortwave (SW) and VIS wavelengths. A few studies have estimated the SW cloud albedos from VIS measurements (Wydick et al. 1987; Laszlo et al. 1988; Vesperini and Fouquart 1994). Also, the ad hoc assumption that the VIS ADM is equal to the SW ADM, used in deriving VIS albedos from VIS reflectance measurements (Gutman 1994; Li et al. 1997b), needs testing.

In this study, 1-yr of ScaRaB radiance measurements were employed to establish SW and VIS ADMs for various types of overcast scenes and examine their dependence on cloud properties. Uncertainties in SW TOA albedos due to angular conversion are evaluated. Five ADMs were developed for overcast scenes including one for all overcast scenes, and four subsets of specific overcast scenes, namely, thin, thick, warm, and cold overcast scenes. Thin and thick clouds were differentiated using ScaRaB VIS measurements, while cold and warm clouds were separated based on the IR brightness temperatures. These ADMs were compared with each other and to the ERBE overcast ADM. The comparison helps to assess the accuracy in the TOA albedo–flux conversions. Note that the current ScaRaB flux–albedo products were generated using the ERBE ADMs and its scene identification scheme. The biases in TOA albedos inverted by applying a single mean overcast ADM are evaluated for thin, thick, warm, and cold clouds. The discrepancies between the ADMs for specific cloud types are discussed and compared to model simulations.

The following section describes the ScaRaB data and analysis procedures. The third section compares between the ScaRaB ADM and ERBE ADM, SW ADM, and VIS ADM, and between the mean overcast ADM and ADMs for subsets thin, thick, warm, and cold overcast scenes. Differences in albedos resulting from the use of different ADMs are also discussed in this section. Section 4 attempts to understand the ADM differences by means of modeling. The last section summarizes the study.

2. Data analysis

a. ScaRaB A2 data

The ScaRaB project was a cooperative space mission by France, Russia, and Germany. Approximately 1 yr of ScaRaB data from March 1994 to February 1995 was acquired before it ceased functioning. The ScaRaB radiometers were on board the Russian meteorological satellite *Meteor-3/7* (Kandel et al. 1998). Like other ERB missions, ScaRaB data were calibrated on board. The polar orbiting *Meteor-3/7* has a non-sun-synchronous orbit with an inclination angle of 82.5°, which is different from the sun-synchronous *Nimbus-7* and the ERBE aboard the NOAA satellites. It allows for observations at various illuminating and observing angles.

The data products used here are the ScaRaB A2 level, which is comparable to the ERBE Processed Archival Tapes (PAT or S-8) dataset. The ScaRaB instrument is a four-channel cross-track scanning radiometer with an instantaneous nadir field of view of ~60 km. There are 51 pixels per scan line with maximum viewing zenith angles around 65°. The four channels include VIS (0.55–0.65 μm) and IR (10.5–12.5 μm) narrowband channels and the SW (0.2–4 μm) and total (0.2–50 μm) broadband channels. The quality of the ScaRaB data has been evaluated using ground-based (Mueller et al. 1997) and spaceborne observations from multiple sensors (Raison and Kandel 1995; Kandel et al. 1998), as well as intercomparisons with independent synergetic data (Trishchenko and Li 1998). The differences in fluxes between the ScaRaB and Earth Radiation Budget Satellite (ERBS) nonscanning radiometers are within 0.76 $\pm$ 5.50 W m^{-2} for SW radiation (Bess et al. 1997), which are comparable to the differences between the ERBE scanner and nonscanner data (Green et al. 1990). The estimated calibration uncertainty is less than 1% for the SW channel and ~1%–2% for the visible channel.

b. Data sampling

Using satellite observations to estimate an ADM and the associated uncertainty, it is important to reduce the autocorrelation in the measurements (Li and Leighton 1992). Since the ScaRaB A2 data product recorded every eight scan lines in a data record, the data sampling was made first by skipping every other data record. Each of the data records contained 408 pixels from eight consecutive scan lines, and covered a geographical frame of approximately 250 km × 3500 km, (8 pixels in scan line direction × 51 pixels in scan spot direction). Within each sampled frame, ScaRaB pixels were grouped into different angular bins of solar zenith angle (SZA) θ_0, satellite viewing zenith angle (VZA) θ, and relative azimuth angle (RAA) ϕ, between the sun and satellite.

TABLE 1. Angular bins used by ERBE ADMs.

No.	Solar zenith angle (θ_0)	No.	Viewing zenith angle (θ)	No.	Relative azimuth angle (ϕ)
1	0.00°–25.84°	1	0°–15°	1	0°–9°
2	25.84°–36.87°	2	15°–27°	2	9°–30°
3	36.87°–45.57°	3	27°–39°	3	30°–60°
4	45.57°–53.13°	4	39°–51°	4	60°–90°
5	53.13°–60.00°	5	51°–63°	5	90°–120°
6	60.00°–66.42°	6	63°–75°	6	120°–150°
7	66.42°–72.54°	7	75°–90°	7	150°–171°
8	72.54°–78.46°			8	171°–180°
9	78.46°–84.26°				
10	84.26°–90.00°				

The angular bins are defined in Table 1, following the development of ERBE ADMs (Suttles et al. 1988). Due to the maximum VZA of the ScaRaB scanner being around 65°, only 10 valid VZA bins (5 in forward and 5 in backward scanning modes) were obtained within a sampled frame for up to VZA = 63°. The 10 VZA bins from limb to limb were further sampled by skipping every other VZA bin. Skipping of odd or even numbers of the VZA bins was switched between every other sampled frame to avoid gaps in VZA bins. The overcast pixels identified within each sampled angular bin were then averaged, yielding a single overcast sample within the angular bin. As one VZA bin covered about five scanning pixels, the data samples obtained by skipping every other VZA bin and every other frame were at least 250 km apart, which were taken to be independent samples.

The identification of the ScaRaB overcast pixels was conducted following the maximum likelihood estimation (MLE) of the ERBE scene identification method (Wielicki and Green 1989), as described by Viollier et al. (1995). Although being a powerful statistical method (Kendall and Stuart 1967), the use of ERBE MLE method for ScaRaB scene identification is still subject to errors, due to the coarse resolution of the SW and LW radiance measurements and the increase of ScaRaB pixel size from nadir to limb. The potential biases in the derived overcast ADMs resulting from inaccurate scene identification will be discussed later.

Table 2 shows the numbers of the overcast samples obtained for two SZA bins (0°–25.8° and 72.5°–78.5°) and all available VZA and RAA bins, together with the associated means and standard deviations of the overcast SW and VIS reflectances and IR brightness temperatures for various angular bins. The results were obtained for overcast scenes over all types of surface background. Fewer samples were collected for smaller SZAs than for larger SZAs. This is because the ScaRaB observations for smaller SZAs were made only at low latitudes, whereas observations for larger SZAs were from all latitudes. Fewer samples in the principal plane (RAA 0°–9° and 171°–180°) are due to smaller bin sizes. The mean SW and VIS reflectances of the angular bins are
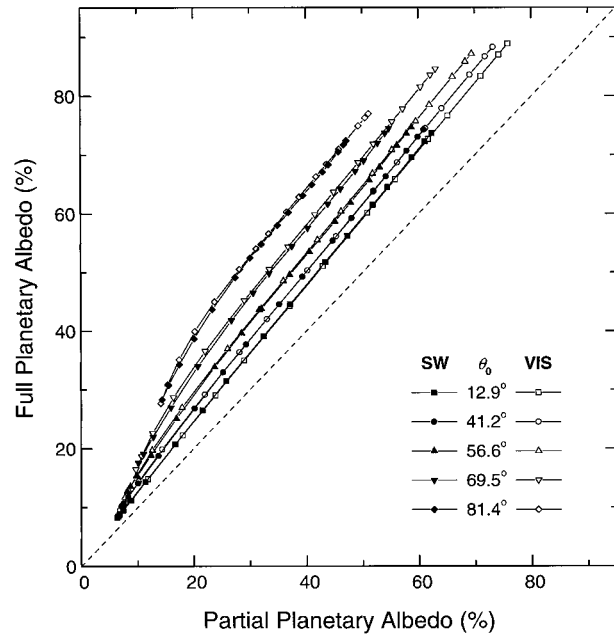

FIG. 1. Relationship between full and partial planetary albedos (%) for both SW and VIS and five SZAs from model calculations. The points are for different visible cloud optical depth range from 0.2–512.

used to derive the overcast ADMs for SW and VIS. Uncertainties in the sampled means are estimated by the standard error at a 95% significance level. For both SW and VIS reflectances, the uncertainties are around 0.01–0.015 at small SZAs and 0.005 at large SZAs; for IR temperatures, they are ~1–2 K at small SZAs and 0.5 K at large SZAs.

c. Selections of thin, thick, warm, and cold overcast scenes

To investigate grossly the dependence of the overcast ADMs on cloud properties, the overcast samples were further separated into four groups, that is, thin clouds versus thick clouds, and warm clouds versus cold clouds. The first separation helps evaluate the dependence of ADMs on cloud optical depth, while the second, on cloud water phase. Following Loeb and Coakley (1998), thin and thick clouds were distinguished according to the percentiles of ScaRaB overcast VIS reflectances observed at each angular bin. In the analysis, the thin cloud scenes consist of the 5th–30th thinnest percentiles in the VIS reflectances, whereas the thick clouds encompass the 70th–95th percentiles. Data falling outside of the 5th–95th percentile were eliminated to reduce the influence of outlying extreme values. The mean reflectances for the selected thin clouds were smaller by about 30%–35% at small SZAs and 20% at large SZAs than the overall mean reflectances (cf. Table 2), whereas for the thick clouds, they were larger than the overall means by the similar magnitudes. The mean

TABLE 2. Statistics of the overcast samples for each angular bin, including the number of samples (top), mean SW (2nd), and VIS (3d) reflectances (%) and mean IR brightness temperature (K) (bottom). In the parentheses are standard deviations. Results are shown for two SZA bins.

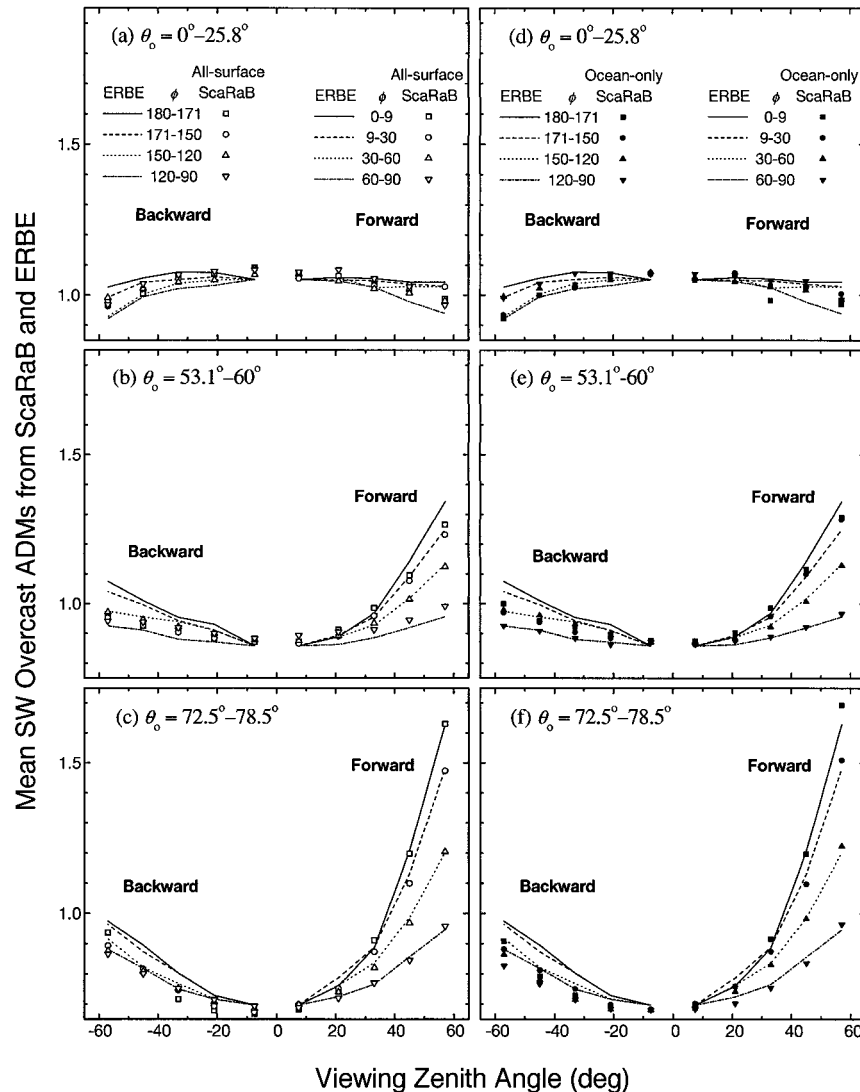|		RAA bins							
		0°–9°	9°–30°	30°–60°	60°–90°	90°–120°	120°–150°	150°–171°	171°–180°
SZA Bin 1 0°–25.8°	VZA 0–15%	204	423	573	643	584	686	599	299
		45.4 (10.4)	44.8 (10.9)	45.4 (11.2)	45.7 (10.5)	46.0 (10.8)	45.3 (11.0)	46.2 (10.6)	46.3 (11.0)
		50.7 (12.6)	50.2 (13.5)	50.9 (13.8)	51.1 (13.0)	51.5 (13.3)	50.7 (13.5)	51.7 (13.1)	51.9 (13.6)
		252.3 (12.4)	251.7 (11.4)	251.0 (12.4)	252.6 (11.6)	252.6 (12.3)	252.6 (12.0)	252.1 (12.6)	252.2 (12.4)
	VZA 15°–27°	163	339	540	497	438	491	354	177
		45.2 (11.5)	45.2 (10.3)	44.4 (10.7)	46.0 (10.5)	45.8 (9.9)	44.6 (11.5)	45.5 (11.0)	45.4 (11.8)
		50.6 (14.0)	50.5 (12.9)	49.6 (13.4)	51.5 (12.9)	51.2 (12.0)	49.5 (14.0)	50.7 (13.6)	50.6 (14.3)
		252.5 (14.5)	252.5 (13.7)	251.7 (11.9)	252.2 (12.1)	252.5 (12.1)	252.0 (12.2)	251.0 (12.0)	251.0 (11.6)
	VZA 27°–39°	198	371	601	536	477	503	373	153
		44.0 (10.9)	43.8 (10.2)	43.3 (9.8)	44.8 (10.0)	45.3 (10.0)	44.3 (10.7)	44.7 (11.6)	45.0 (11.2)
		48.7 (13.5)	48.7 (12.5)	48.2 (12.0)	49.8 (12.3)	50.5 (12.3)	49.1 (13.0)	49.7 (14.2)	50.0 (13.8)
		249.3 (11.7)	250.4 (11.5)	251.6 (11.2)	251.7 (11.8)	252.3 (12.7)	250.7 (12.3)	250.0 (12.3)	250.4 (12.6)
	VZA 39°–51°	177	400	597	562	547	531	339	173
		43.3 (10.2)	43.9 (9.0)	42.7 (9.2)	43.7 (9.3)	44.1 (9.5)	43.4 (9.8)	43.3 (10.2)	42.6 (10.1)
		48.0 (12.6)	48.6 (11.2)	47.1 (11.3)	48.3 (11.5)	48.8 (11.7)	47.8 (11.9)	47.7 (12.5)	46.9 (12.3)
		247.2 (10.6)	247.8 (11.0)	249.6 (10.8)	250.4 (12.0)	250.5 (12.5)	249.2 (11.8)	248.3 (11.8)	249.4 (10.8)
	VZA 51°–63°	225	484	662	627	551	554	365	162
		42.0 (8.7)	43.6 (9.1)	41.6 (8.2)	41.0 (8.7)	41.1 (9.2)	42.1 (8.8)	40.9 (10.1)	41.6 (9.5)
		45.4 (10.6)	47.7 (11.0)	45.5 (10.0)	44.7 (10.5)	44.9 (11.1)	45.9 (10.6)	44.5 (12.1)	45.5 (11.5)
		246.2 (10.7)	246.5 (11.7)	248.5 (10.8)	249.1 (11.0)	249.7 (11.6)	248.1 (12.9)	247.0 (10.8)	247.1 (10.9)
SZA Bin 8 72.5°–78.5°	VZA 0°–15°	572	1745	1916	1951	1480	2210	2034	961
		44.0 (6.2)	45.1 (6.3)	45.1 (6.9)	44.5 (6.6)	44.8 (6.8)	44.2 (6.7)	43.6 (6.7)	43.1 (6.7)
		47.1 (7.3)	48.6 (7.8)	49.0 (8.8)	48.4 (8.6)	49.2 (9.1)	48.1 (8.7)	47.0 (8.3)	46.2 (8.1)
		249.6 (11.4)	251.8 (9.5)	252.2 (8.8)	252.1 (8.4)	253.0 (8.3)	252.0 (8.9)	251.8 (9.0)	251.6 (10.2)
	VZA 15°–27°	564	1455	1568	1127	1051	1579	1422	423
		48.0 (6.4)	48.5 (6.6)	47.8 (6.7)	46.4 (6.8)	46.1 (6.1)	45.7 (6.6)	44.8 (5.8)	43.8 (6.2)
		50.1 (7.6)	52.0 (8.2)	51.4 (8.6)	50.9 (9.0)	51.1 (8.4)	50.1 (8.8)	48.2 (7.3)	46.7 (7.5)
		250.7 (10.7)	251.5 (9.5)	251.5 (8.3)	252.2 (7.9)	253.0 (7.5)	252.5 (8.6)	252.0 (9.0)	249.6 (10.9)
	VZA 27°–39°	953	1632	1637	1106	1104	1594	1566	372
		58.9 (7.3)	56.4 (7.1)	52.9 (7.2)	49.7 (6.6)	48.5 (6.1)	48.6 (6.7)	48.2 (6.2)	46.2 (6.7)
		61.4 (8.7)	59.8 (8.8)	56.1 (8.7)	54.2 (9.0)	53.4 (8.1)	53.1 (8.9)	51.5 (7.8)	49.1 (8.2)
		249.7 (11.3)	250.2 (9.3)	250.5 (8.7)	251.4 (8.3)	252.2 (8.4)	251.4 (9.7)	251.6 (9.0)	249.1 (11.5)
	VZA 39°–51°	1872	1945	1876	1167	1109	1588	1712	490
		77.4 (8.4)	71.0 (8.4)	62.5 (7.7)	54.6 (6.2)	51.7 (5.7)	52.2 (6.3)	52.7 (6.2)	52.2 (7.2)
		80.0 (9.8)	74.0 (9.6)	65.1 (9.0)	58.3 (8.3)	56.2 (7.6)	56.2 (8.2)	55.9 (7.7)	55.6 (8.8)
		247.1 (11.1)	246.9 (10.2)	248.5 (9.2)	250.0 (7.9)	251.5 (8.5)	250.9 (10.0)	251.0 (9.0)	248.8 (11.1)
	VZA 51°–63°	2987	2193	1988	1205	1110	1608	1623	1009
		105.6 (13.0)	95.1 (13.1)	77.8 (9.2)	61.8 (6.7)	55.9 (5.4)	56.6 (6.0)	57.7 (6.1)	60.5 (5.7)
		106.1 (11.3)	96.6 (12.0)	79.0 (9.6)	64.4 (8.4)	59.3 (7.3)	59.6 (7.5)	60.2 (7.3)	63.7 (6.9)
		246.2 (9.8)	245.5 (9.0)	246.8 (9.2)	248.9 (8.5)	250.3 (8.8)	250.4 (10.2)	249.8 (9.7)	249.1 (10.4)

FIG. 2. Comparison between ScaRaB all-surface and ERBE SW overcast ADMs (left panels) and between ScaRaB ocean-only and ERBE overcast ADMs (right panels) for three SZA bins. Forward scattering denoted by positive VZAs for RAAs 0°–90°; backward scattering denoted by negative VZAs for RAAs 90°–180°.

IR brightness temperatures for the thin and thick clouds were very close. The differences were generally 0–3 K.

The same threshold percentiles were employed to distinguish between warm and cold clouds based on the statistics of the ScaRaB IR brightness temperatures observed at each angular bin. The mean temperatures for the warm clouds were larger by about 10–15 K at small SZAs and 10 K at large SZAs than the overall mean overcast temperatures (cf. Table 2), whereas for the cold clouds, their mean temperatures were smaller than the overall metals by the similar magnitudes. For the relatively warm and cold IR temperature (different by ~20–25 K), the selected warm clouds and cold clouds were assumed to consist primarily of water droplets and ice crystals, respectively.

3. Development and comparisons of ADMs

a. Development of ADMs

A set of SW overcast ADMs, like the ERBE ones, was generated using ScaRaB data based on the angular-bin mean SW overcast reflectances described previously. An ADM, R, is defined by (Suttles et al. 1988)

$$R(\theta_0, \, \theta, \, \phi) = \frac{a(\theta_0, \, \theta, \, \phi)}{A(\theta_0)}, \qquad (1)$$

where a denotes the reflectance as a function of θ_0, θ, and ϕ and A denotes the planetary albedo as a function of θ_0 only. The planetary albedo A is defined by

$$A(\theta_0) = \frac{1}{\pi} \int_0^{2\pi} d\phi \int_0^{\pi/2} d\theta\, a(\theta_0, \theta, \phi)\cos\theta\sin\theta. \quad (2)$$

Since the ScaRaB instrument did not provide observations at very large VZAs ($\theta > 65°$), a partial planetary albedo, A_p, was calculated first by (Li 1996)

$$A_p(\theta_0) = \frac{1}{\pi} \int_0^{2\pi} d\phi \int_0^{\alpha} d\theta\, a(\theta_0, \theta, \phi)\cos\theta\sin\theta. \quad (3)$$

In the equation, $[0, \alpha]$ denotes the valid VZA domain where ScaRaB observations were available. Using the finite angular bins and corresponding mean reflectances at valid VZA bins, the integrals in Eq. (3) can be calculated by the following summations:

$$\sum_{k=1}^{8} (\phi_{k+1} - \phi_k) \sum_{j=1}^{5} \bar{a}_{ijk}(\sin^2\theta_{j+1} - \sin^2\theta_j), \quad (4)$$

where i, j, and k represent, respectively, the SZA, VZA, and RAA bin numbers and $\bar{a}_{ijk}$ denotes the mean reflectance at discrete bins. For the angular bins used here (see Table 1), $k = 1, 2, \ldots, 8$ are for $\phi = [0°, 180°]$ and $j = 1, 2, \ldots, 5$ are for $\theta = [0°, 63°]$.

The full planetary albedo was then estimated from the partial planetary albedo, based on a unique relationship between the two. Figure 1 shows the relationships between the full and partial planetary albedos derived for both SW and VIS wavelengths at various SZAs. These albedos were calculated using a comprehensive radiation model (Chang 1997) for cloud visible optical depths ranging from 0.2 to 512, and the difference between the full and partial planetary albedos increases with increasing SZAs. At specified SZA, such a relationship between the two albedos was found to have very little dependence on either cloud amount, particle size, and water phase or atmospheric aerosol and humidity profiles. Based on model simulations for both homogeneous and inhomogeneous cloud fields, Loeb et al. (2000) estimated the full albedo from the partial albedo and showed that the uncertainties in the estimated albedo are within ±0.01. In the development of the overcast ADMs for SW and VIS wavelengths and for the subsets of thin, thick, warm, and cold overcast scenes, the full planetary albedos were all estimated from the computed partial planetary albedos.

b. Mean SW and VIS overcast ADMs and TOA albedos

Figure 2 shows the comparisons of mean SW overcast ADMs derived from ScaRaB and ERBE as a function of VZA for eight RAA bins. In the left panels, the ScaRaB SW overcast ADMs were derived using observations from overcast scenes over all types of surface background, whereas the right panels were derived from overcast scenes over oceans only. The three subpanels from top to bottom are for three different SZA bins. For both clouds over all surfaces and over oceans only, the
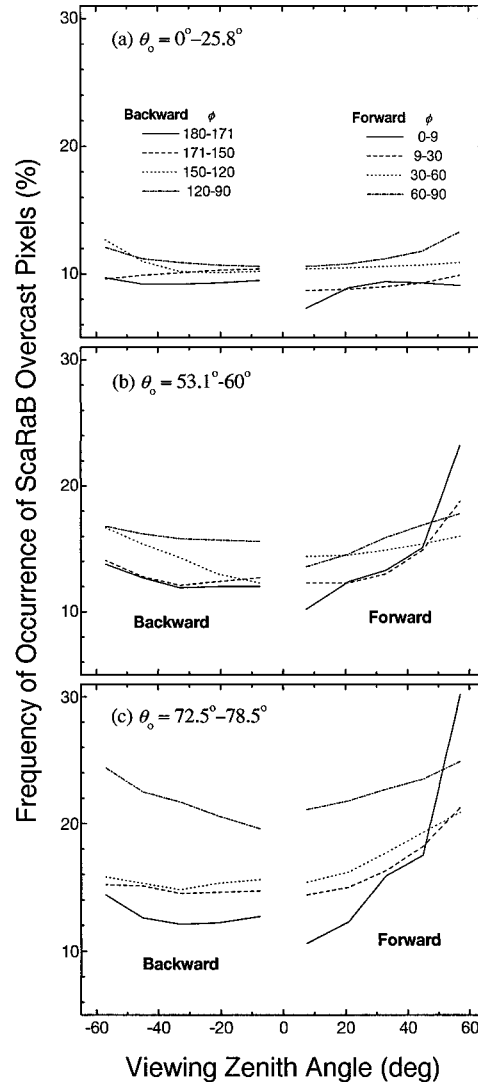

FIG. 3. Frequency of occurrence (%) of ScaRaB overcast pixels for three SZA bins. Forward scattering denoted by positive VZAs for RAAs 0°–90°; backward scattering denoted by negative VZAs for RAAs 90°–180°.

reflection of overhead sun is the closest to isotropic. As the SZA increases, the ADMs exhibit a larger dependence on the viewing geometry. The largest ADM values occur in the principal forward scattering direction (RAA bin 0°–9°) and the ADMs are relatively small, in the sideward scattering directions (RAA bins 60°–90° and 90°–120°). These features are common in all the ADMs under study.

When comparing the ScaRaB ADMs to the ERBE ADMs, the trends are similar, but the ScaRaB ADMs show less dependence on the viewing geometry at median SZAs and in the backward and sideward scattering directions. The largest difference occurs in the backward scattering direction. The discrepancies between the ScaRaB and ERBE ADMs may be attributed to biases
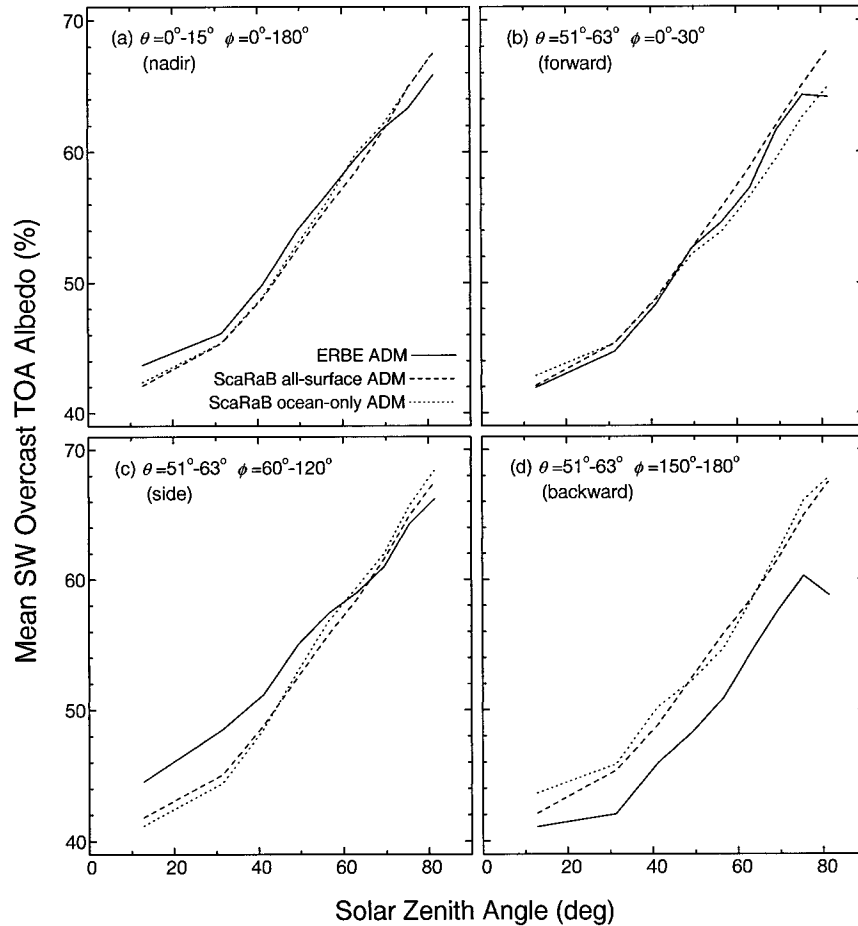
FIG. 4. Comparison of the mean SW overcast TOA albedos derived based on the ERBE (solid), ScaRaB all-surface (dashed), and ScaRaB ocean-only (dotted) ADMs as a function of SZA. Results are presented for nadir, forward, sideward, and backward viewing directions.

in the overcast scene identification. As ERBE ADMs were primarily built based on *Nimbus-7* data with a constant footprint for all VZAs, the ScaRaB pixel resolutions growing from ~60 km at nadir to over 200 km at limb could induce biases in the overcast scene identification due to broken cloud contamination.

Figure 3 shows the frequencies of occurrence of ScaRaB overcast pixels as identified by the MLE method at different viewing geometries. The frequency increased drastically with increasing SZA, and with increasing VZA for larger SZAs in the forward and sideward scattering directions. Since the frequency should be statistically independent of viewing geometry, biases in the scene identification are evident given that many broken clouds may be misidentified as overcast, leading to less limb brightening in the ScaRaB ADMs. Ye and Coakley (1996), using ERBE data, evaluated such scene identification biases based on a comparison between the anisotropy factors for constant-sized fields of view and unaltered full-resolution fields of view. They found significant differences on the order of 5%–10% for all

scene types. Averaging over large geometric sizes of the ScaRaB pixels at large VZAs may be another cause for the more isotropic ScaRaB ADMs (Li 1996).

As for the effect of the background surface, ScaRaB overcast ADMs constructed over all surface types and over oceans only appear to be very similar, implying that overcast clouds were thick enough so that the underlying surface had little impact on the TOA ADM. However, one difference is significant in the forward scattering direction at large SZAs where clouds over oceans were a little brighter than clouds over all surface types, which may be caused by the sunglint effect over ocean surface.

Figure 4 shows the comparisons of the mean SW overcast TOA albedos derived from three different overcast ADMs, that is, ERBE SW ADM and two ScaRaB SW ADMs for all types of surface background and for oceans only, as a function of SZA. The albedos, calculated for overcast scenes over all surface backgrounds, are presented for four different viewing–scattering directions, namely, nadir, forward, sideward, and
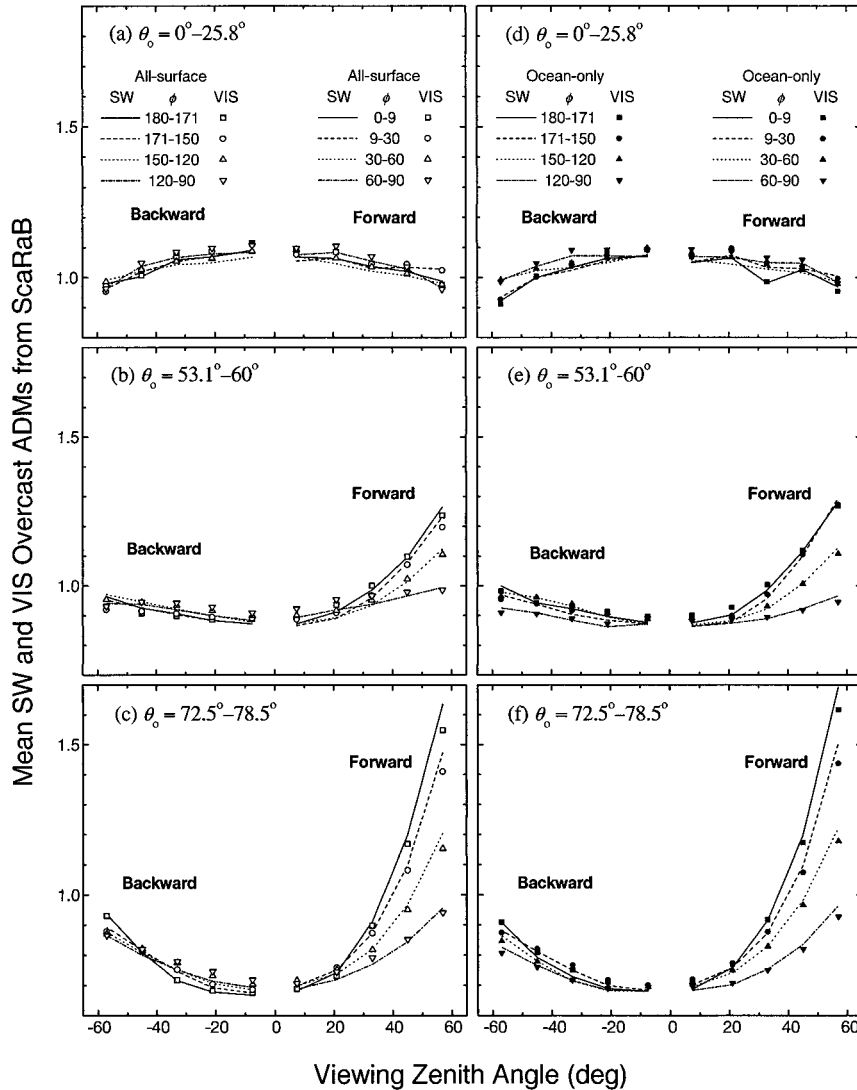
FIG. 5. Same as Fig. 2, but for the comparisons of ScaRaB SW and VIS overcast ADMs
derived from all types of surface background (left panels) and from oceans only (right panels).

backward. The mean albedos are the averages of different RAA bins, weighted by the number of samples in each RAA bin. The albedos derived from the ERBE ADM differ largely from those derived based on the ScaRaB ADMs at many scattering directions. As manifested in Fig. 2, ERBE ADM shows more anisotropy when compared to the ScaRaB ADMs. Thus, a smaller ERBE ADM value in the sideward scattering direction converts the reflectance to a larger albedo than the ScaRaB ones, whereas a larger ERBE ADM value in the backward scattering direction converts the reflectance to a smaller albedo. As manifested in Fig. 4, the ERBE and ScaRaB albedos generally have the largest difference in the backward scattering direction ($\sim$0.04), while at the nadir and forward directions, the albedo differences are small ($<$0.01).

Figure 4 also shows that mean albedos derived from the ScaRaB ADMs for all surface types and for oceans only are much closer except for forward scattering directions at large SZAs, where the mean albedos derived using the all-surface ADM are larger. This is because the all-surface ADM is smaller than the oceans-only ADM at these scattering directions.

The ScaRaB overcast ADMs for the VIS channel were also constructed for both all surfaces and oceans only. Figure 5 shows the comparisons between ScaRaB VIS and SW overcast ADMs for three SZA bins. For both all-surface (Figs. 5a and 5b, and 5c) and ocean-only (Figs. 5d and 5e, and 5f) ADMs, ScaRaB VIS and SW ADMs bear very close resemblance, with the VIS ADM being a little larger at nadir and smaller at limb. The maximum albedo biases for using a SW ADM to convert
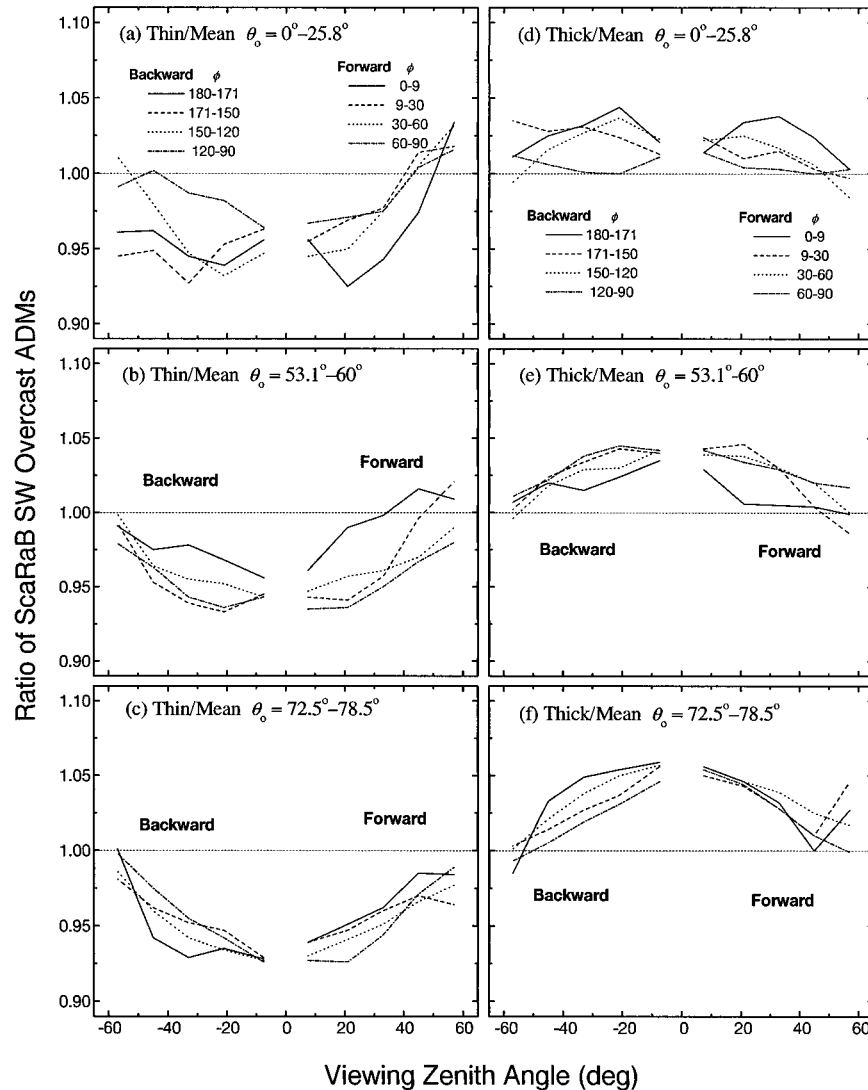
FIG. 6. Ratios of the ScaRaB thin to mean (left panels) and thick to mean (right panels) SW overcast ADMs for three SZA bins. Forward scattering denoted by positive VZAs for RAAs 0°–90°; backward scattering denoted by negative VZAs for RAAs 90°–180°.

VIS reflectance to albedo are around 0.05 at these extreme VZAs, but the mean bias averaged over all view direction is small (<0.01).

c. Thin, thick, warm, and cold overcast ADMs and TOA albedos

Shortwave overcast ADMs for thin and thick clouds were generated and compared with the mean SW overcast ADM for all clouds. Figure 6 shows the ratios of thin and thick overcast ADMs to the mean overcast ADM for three SZA bins. The thin overcast ADM is generally smaller at small VZAs and tends to be larger at large VZAs than the mean overcast ADM; the opposite is true for thick overcast clouds. Such a contrast between the thin and thick overcast ADMs is expected,

as reflection by thinner clouds bears more resemblance to the characteristics of low-order scattering, which exhibits stronger angular dependence. On the other hand, photons traveling through a thick cloud undergo many scattering events and so smooth out the angular dependence. Therefore, thick clouds have more isotropic reflection (Suttles 1981). In Fig. 6, the range of the ratios for thick ADMs is less than 0.05, and for thin ADMs, the range is up to 0.1. The fluctuation of the ratios also decreases with increasing SZA in the forward-scattering direction. At larger SZAs, there is less RAA dependence in the forward reflectances for both thin and thick clouds.

Similar comparisons between the warm and cold overcast ADMs are shown in Fig. 7. They display more complicated features, which are attributed to the larger
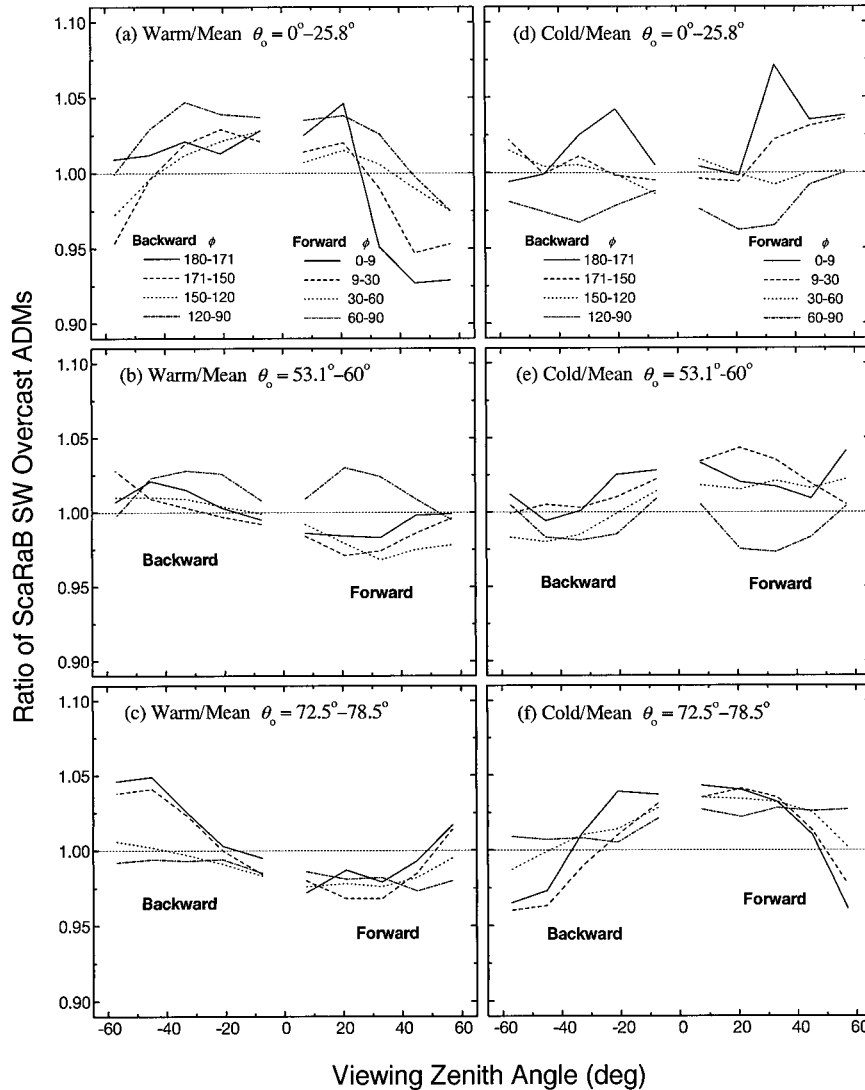
FIG. 7. Same as Fig. 6, but for ratios of ScaRaB warm to mean (left panels) and cold to mean (right panels) SW overcast ADMs.

differences in the scattering phase functions between water droplets and ice particles (cf. section 4 for more details). For example, for a SZA of 10° and VZAs = 0°–63°, the scattering angle Θ, defined by

$$\cos\Theta = \cos\theta_0 \cos\theta + \sin\theta_0 \sin\theta \cos\phi, \qquad (5)$$

ranges from about 110° to 170° for RAAs = 0°–90°, and from about 130° to 180° for RAAs = 90°–180°. For a SZA of 75° and VZAs = 0°–63°, the scattering angle ranges from about 55° to 105° for RAAs = 0°–90°, and from about 115° to 165° for RAAs = 90°–180°. Both theories and observations show large discrepancies between the scattering phase functions for water and ice clouds at these scattering angles (Liou 1992; Heymsfield and Miloshevich 1993; Takano and Liou 1995; Macke et al. 1996).

As shown in Fig. 7, warm cloud ADMs appear brighter than cold cloud ADM in a direct backscattering di-

rection ($\Theta \approx 180°$), but darker at $\Theta \approx 100°$. Note that $\Theta \approx 180°$ corresponds to similar VZA and SZA in the backward scattering direction, while $\Theta \approx 100°$ corresponds to a VZA $\approx (20°, 26.9°)$ for SZA = 53.1°–60° in the forward scattering direction (middle panels), and at a nadir SZA = 72.5°–78.5° (bottom panels). The deviations of the warm and cold cloud ADMs from the mean ADM are generally less than 5%.

The discrepancies in the ADMs lead to bias errors in the estimation of albedos if one applies the mean overcast ADM to the specific thin, thick, warm, and cold clouds. Figure 8 shows the comparisons of mean SW TOA albedos as a function of SZA derived separately based on the mean overcast ADM (solid) and the ADMs for thin (dash dot), thick (dash dot dot), warm (dash), and cold (dot) clouds for their respective cloud subsets. The results are presented for four different viewing/scattering directions, like in Fig. 4. In general, the use
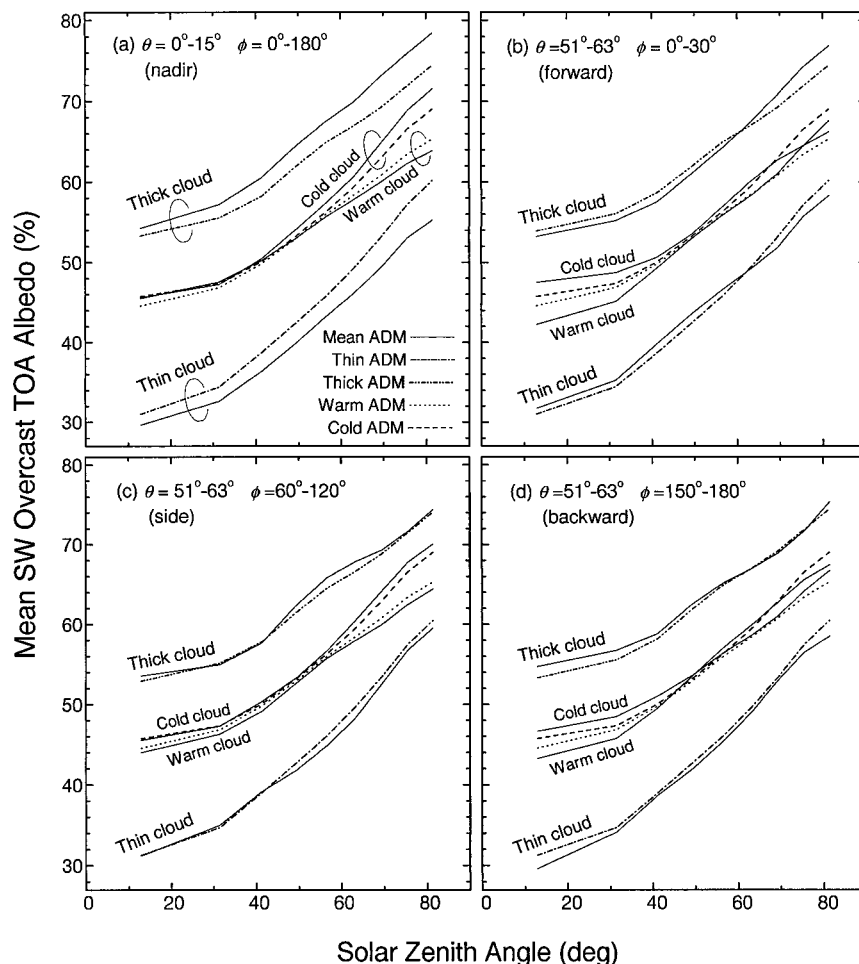
FIG. 8. Comparison of the mean SW overcast TOA albedos for thin, thick, warm, and cold clouds derived based on the overall mean ADM (solid) and specific thin (dash dot), thick (dash dot dot), warm (dot), and cold (dash) ADMs. Results are presented for nadir, forward, sideward, and backward viewing directions.

of a single mean overcast ADM gives rise to albedo bias errors of ~0.01–0.04. The biases are larger at nadir VZAs for both thin and thick clouds. At $\theta = 51°–63°$, the biases are smaller with a similar magnitude in all forward, sideward, and backward scattering directions. The overall mean differences averaged over all angular bins ($\theta_0 = 0°–84.3°$, $\theta = 0°–63°$, $\phi = 0°–180°$) are less than 0.005 for all cloud types under study.

4. Comparison between observation and modeling

To investigate to what degree a radiative transfer model can account for the differences in ADMs for various cloud scenes, an adding–doubling model was used to simulate the reflectances of the thin, thick, warm, and cold clouds at VIS wavelength. Mie theory was adopted to calculate the reflectances for thin and thick clouds, as well as for warm water clouds. A gamma size distribution with a droplet effective radius of

10 μm and an effective variance of 0.13 was used (Hansen 1971). For cold ice clouds, the cirrostratus model presented by Takano and Liou (1989) was chosen. A particle equivalent diameter of 100 μm was used. LOWTRAN-7 model (Kneizys et al. 1988) with a standard midlatitude summer atmosphere (McClatchey et al. 1972) was adopted to account for atmospheric absorption and scattering effects. The cloud layer was placed between 2 and 4 km with a relative humidity of 100%. Cloud optical depths were retrieved from ScaRaB VIS reflectances. Note that the retrieved cloud optical depths showed a large dependence on viewing geometry. Mean cloud optical depths averaged over all VZA and RAA bins were derived for the thin, thick, warm, and cold clouds, respectively. The retrieval was done with lookup tables obtained from radiative transfer calculations at 16 Gaussian quadrature points in the zenith direction (16 up and 16 down), 19 RAAs, and 20 VIS cloud optical depths (Chang 1997). A Lam-
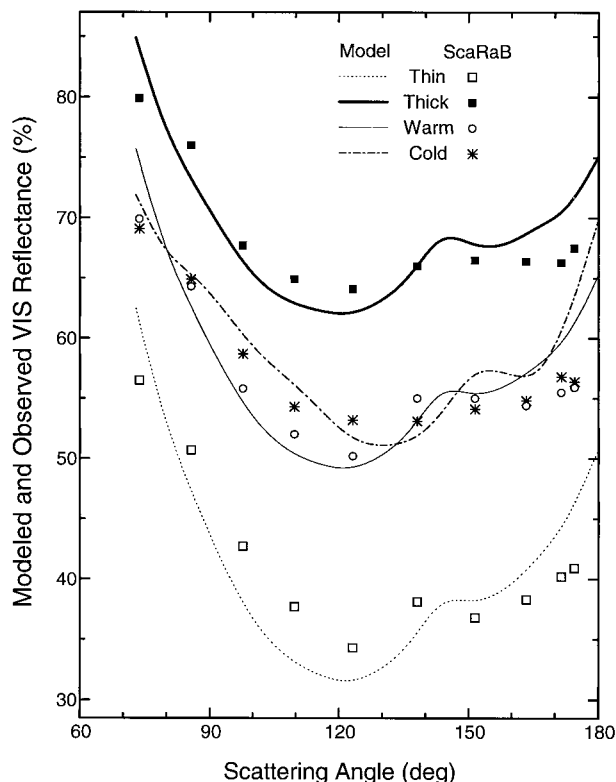
FIG. 9. Comparison of the variations of modeled and observed VIS reflectances as a function of the scattering angle for thin, thick, warm, and cold clouds. Results were obtained for the principal scattering direction with $\theta_0 \approx 49°$.

bertian reflectance of 0.06 for the ocean surface was assumed (Payne 1972).

Figure 9 shows the comparison between model-simulated and ScaRaB-observed VIS reflectances for an SZA of 49° as a function of the scattering angle. The simulated reflectances were obtained for the principal plane (RAAs = 0° and 180°). The ScaRaB VIS reflectances were the averages obtained for the SZA bin of 45.6°–53.1° and RAA bins of 0°–9° and 171°–180°. In general, model simulations induced strong angular variations, due to biases in the plane-parallel radiative transfer calculations (Loeb and Coakley 1998). The smoother angular variations in the observations were resulted by averaging. However, the trends in the angular variations of reflectance are similar, as both modeling and observation exhibit more isotropic reflection for thick clouds than for thin clouds and different angular variations between warm water clouds and cold ice clouds. The cold ice clouds also have the most isotropic reflection between $\Theta = 105°$–165° in the observations.

5. Summary and discussions

ADMs are crucial in determining the TOA albedos and radiative fluxes from satellite radiance measure-

ments. The largest uncertainties in deriving instantaneous fluxes arise from the use of existing ADMs such as those designed for ERBE (Wielicki et al. 1995). It is known that ADMs for cloudy scenes depends on many factors pertinent to the micro- and macro properties of a cloud, but few published studies assess quantitatively the uncertainties resulting from the use of a single ADM for all overcast scenes.

The French–Russian–German Scanner for Radiation Budget satellite program offered some unique advantages for addressing ADM-related issues. The orbital configuration in a non-sun-synchronous orbit enables acquisition of observations in a variety of sun-target-satellite geometries, allowing for the development of ADMs. Second, both VIS and broadband SW scanners were onboard the ScaRaB, allowing for the development and comparison of VIS and SW ADMs. Third, better information is available concerning cloud properties from the ScaRaB VIS and infrared (IR) window channels, which can be used to examine the dependence of ADMs on cloud properties.

In light of these advantages, a new set of SW overcast ADMs was first generated using ScaRaB data and was compared with the ERBE ADMs. The two sets of ADMs were similar in their angular trend but differ somewhat in their magnitude. The ScaRaB ADM was found to be more isotropic than the ERBE ADM, which was caused by the scene identification errors in the ScaRaB overcast pixels. Misidentification of broken cloud fields as overcast scenes in the ScaRaB data lead to smaller angular variations in ScaRaB ADM. The largest disparity was found at large viewing zenith angles (VZAs) in the sideward scattering direction for high sun and in the backward scattering direction for all SZAs. Differences up to 0.04 were found in mean TOA albedos derived by applying the ERBE and ScaRaB ADMs to the ScaRaB overcast reflectances. The SW overcast ADMs derived over all surface types were very similar to those derived for oceans only, except for the forward scattering at large SZAs The overcast ADM derived for the VIS channel was similar to, but a little brighter at nadir and a little darker at limb than, the SW ADM.

To examine the dependence of cloud SW ADMs on cloud optical properties, overcast scenes were separated into thin and thick clouds based on the ScaRaB VIS reflectances, and warm water clouds and cold ice clouds according to the ScaRaB IR window emission temperatures. The ADMs for these subsets of overcast scenes differ considerably from each other and deviate from the mean ADM for all overcast scenes. In contrast, the thin versus thick overcast ADMs showed opposite deviations from the mean overcast ADM, and likewise the warm versus cold overcast ADMs. Based on the four ADMs for thin, thick, warm, and cold clouds, the use of the mean overcast ADM lead to albedo bias errors of ~0.01–0.04 depending on the characteristics of the overcast scene types (i.e., thin, thick, warm, and cold). Such errors reduced to about 0.005 when averaged over

all cloud types and viewing geometry. These findings demonstrate the importance of generating more sophisticated cloud ADMs that should be functions of at least cloud optical depth and its microphysics.

An attempt was also made to understand the differences from the perspective of radiative transfer modeling. The prominent differences between the water and ice cloud ADMs originate mainly from the different particle scattering phase functions, while the discrepancies between the thin and thick cloud ADMs are associated with the number of photon scattering orders. Low-order scattering leaves more characteristics of the scattering phase function, whereas high-order scattering leads to more isotropic reflection. The general trends of the modeled and observed ADMs are similar, but their detailed features are noticeably different because of limitations of radiative transfer modeling.

REFERENCES

Arking, A., 1991: The radiative effects of clouds and their impact on climate. *Bull. Amer. Meteor. Soc.,* **72,** 795–813.

Barkstrom, B. R., and G. L. Smith, 1986: The Earth Radiation Budget Experiment: Science and implementation. *Rev. Geophys.,* **24,** 379–390.

Bess, T. D., G. L. Smith, R. N. Green, D. A. Rutan, R. S. Kandel, P. Raberanto, and M. Viollier, 1997: Intercomparison of Scanning Radiometer for Radiation Budget (ScaRaB) and Earth Radiation Budget Experiment (ERBE) results. Preprints, *Ninth Conf. on Atmospheric Radiation,* Long Beach, CA, Amer. Meteor. Soc., 203–207.

Capderou, M., 1998a: Determination of the shortwave anisotropic function for clear-sky desert scenes from ScaRaB data: Comparison with models issued from other satellite data. *J. Appl. Meteor.,* **37,** 1398–1411.

——, 1998b: Confirmation of Helmholtz reciprocity using ScaRaB satellite data. *Remote Sens. Environ.,* **64,** 266–285.

Chang, F.-L., 1997: Properties of low-level marine clouds as deduced from AVHRR satellite observations. Ph.D. dissertation, Oregon State University, 335 pp.

——, Z. Li, and S. A. Ackerman, 2000: Examining the relationship between cloud and radiation quantities derived from satellite observations and model calculations. *J. Climate,* **13,** 3842–3859.

Green, R. N., F. B. House, P. W. Stackhouse, X. Wu, S. A. Ackerman, W. L. Smith, and M. J. Johnson, 1990: Intercomparison of scanner and nonscanner measurements for the Earth Radiation Budget Experiment. *J. Geophys. Res.,* **95,** 11 785–11 798.

Gutman, G., 1994: Normalization of multi-annual global AVHRR reflectance data over land surfaces to common sun-target-sensor geometry. *Adv. Space Res.,* **14,** 121–124.

Hansen, J. E., 1971: Multiple scattering of polarized light in planetary atmospheres. Part II: Sunlight reflected by terrestrial water clouds. *J. Atmos. Sci.,* **28,** 1400–1426.

Hartmann, D. L., V. Ramanathan, A. Berroir, and G. E. Hunt, 1986:

Earth radiation budget data and climate research. *Rev. Geophys.,* **24,** 439–468.

Heymsfield, A. J., and L. M. Miloshevich, 1993: Overview of microphysical state parameter measurements from FIRE II. *FIRE Cirrus Science Conf.,* Breckenridge, CO, FIRE, 1–4.

Kandel, R. S., J.-L. Monge, M. Viollier, L. A. Pakhomov, V. I. Adas'ko, R. G. Reitenbach, E. Raschke, and R. Stuhlmann, 1994: The ScaRaB project: Earth radiation budget observations from *Meteor* satellite. *Adv. Space. Res.,* **14,** 47–57.

——, and Coauthors, 1998: The ScaRaB earth radiation budget dataset. *Bull. Amer. Meteor. Soc.,* **79,** 765–783.

Kendall, M. G., and A. Stuart, 1967: *The Advanced Theory of Statistics. Vol. 2: Inference and Relationship.* Hafner Publisher Co., 690 pp.

Kneizys, F. X., E. P. Shettle, L. W. Arbeu, J. H. Chetwynd, G. P. Anderson, W. O. Gallery, J. E. A. Selby, and S. A. Clough, 1988: Users guide to LOWTRAN-7. Air Force Geophys. Lab. Tech. Rep. AFGL-TR-88-0177, 137 pp.

Laszlo, I., H. Jacobowitz, and A. Gruber, 1988: The relative merits of narrowband channels for estimating broadband albedos. *J. Atmos. Oceanic Technol.,* **5,** 757–773.

Li, Z., 1996: On the angular correction of satellite radiation measurements: The performance of ERBE angular dependence model in the Arctic. *Theor. Appl. Climatol.,* **54,** 235–248.

——, and H. G. Leighton, 1992: Narrowband to broadband conversion with spatially autocorrelated reflectance measurements. *J. Appl. Meteor.,* **31,** 421–432.

——, L. Moreau, and A. Arking, 1997a: On solar energy disposition: A perspective from observation and modeling. *Bull. Amer. Meteor. Soc.,* **78,** 53–70.

——, ——, and J. Cihlar, 1997b: Estimation of the photosynthetically active radiation absorbed at the surface over the BOREAS region. *J. Geophys. Res.,* **102,** 29 717–29 727.

Liou, K. N., 1992: *Radiation and Cloud Processes in the Atmosphere: Theory, Observation, and Modeling.* Oxford University Press, 487 pp.

Loeb, N. G., and J. A. Coakley Jr., 1998: Inference of marine stratus cloud optical depths from satellite measurements: Does 1D theory apply? *J. Climate,* **11,** 215–233.

——, F. Parol, J.-C. Buriez, and C. Vanbauce, 2000: Top-of-atmosphere albedo estimation from angular distribution models using scene identification from satellite cloud property retrievals. *J. Climate,* **13,** 1269–1285.

Macke, A., J. Mueller, and E. Raschke, 1996: Single-scattering properties of atmospheric ice crystals. *J. Atmos. Sci.,* **53,** 2813–2825.

Manalo-Smith, N., G. L. Smith, S. N. Tiwari, and W. F. Staylor, 1998: Analytic forms of bidirectional reflectance functions for application to earth radiation budget studies. *J. Geophys. Res.,* **103,** 19 733–19 751.

McClatchey, R. A., R. W. Fenn, J. E. Selby, F. E. Volz, and J. S. Garing, 1972: *Optical Properties of the Atmosphere.* Air Force Cambridge Research Laboratories, 108 pp.

Mueller, J., and Coauthors, 1997: Ground characterization of the Scanner for Radiation Budget (ScaRaB) Flight Model 1. *J. Atmos. Oceanic Technol.,* **14,** 802–813.

Payne, R. E., 1972: Albedo of the sea surface. *J. Atmos. Sci.,* **29,** 959–970.

Raison, F., and R. Kandel, 1995: Verifying shortwave in-flight calibration of the ScaRaB/Meteor radiation budget scanner. *Passive Infrared Remote Sensing of Clouds and the Atmosphere,* D. K. Lynch, Ed., SPIE, 367–374.

Smith, G. L., R. N. Green, E. Raschke, L. M. Avis, J. T. Suttles, B. A. Wielicki, R. Davies, 1986: Inversion methods for satellite studies of the earth's radiation budget: Development algorithms for the ERBE mission. *Rev. Geophys.,* **24,** 407–421.

Suttles, J. T., 1981: Anisotropy of solar radiation leaving the earth–atmosphere system. Ph.D. dissertation, Old Dominion University, 180 pp.

——, and Coauthors, 1988: Angular radiation models for earth–atmosphere system. Vol. I—Shortwave radiation. NASA Ref. Publ. 1184, 144 pp.

Takano, Y., and K. N. Liou, 1989: Radiative transfer in cirrus clouds. Part I. Single-scattering and optical properties of hexagonal ice crystals. *J. Atmos. Sci.,* **46,** 3–19.

——, and ——, 1995: Radiative transfer in cirrus clouds. Part III: Light scattering by irregular ice crystals. *J. Atmos. Sci.,* **52,** 818–837.

Trishchencko, A. P., and Z. Li, 1998: Use of ScaRaB measurements for validating a GOES-based TOA radiation product. *J. Appl. Meteor.,* **37,** 591–605.

Vesperini, M., and Y. Fouquart, 1994: Determination of broadband shortwave fluxes from Meteosat visible channel by comparison to ERBE. *Beitr. Phys. Atmos.,* **67,** 121–131.

Viollier, M., R. S. Kandel, and P. Raberanto, 1995: Inversion and space-time averaging algorithms for ScaRaB: Comparison with ERBE. *Ann. Geophys.,* **13,** 959–968.

Wielicki, B. A., and R. N. Green, 1989: Cloud identification for ERBE radiative flux retrieval. *J. Appl. Meteor.,* **28,** 1133–1146.

——, R. D. Cess, M. D. King, D. A. Randall, and E. F. Harrison, 1995: Mission to Planet Earth: Role of clouds and radiation in climate. *Bull. Amer. Meteor. Soc.,* **76,** 2125–2153.

——, B. R. Barkstrom, E. F. Harrison, R. B. Lee III, G. L. Smith, J. E. Cooper, 1996: Clouds and the Earth's Radiant Energy System (CERES): An Earth Observing System experiment. *Bull. Amer. Meteor. Soc.,* **77,** 853–868.

Wydick, J. E., P. A. Davis, and A. Gruber, 1987: Estimation of broadband planetary albedo from operational narrowband satellite measurements. NOAA TR-NESDIS 27, 32 pp.

Ye, Q., and J. A. Coakley Jr., 1996: Biases in earth radiation budget observations. Part 2: Consistent scene identification and anisotropic factors. *J. Geophys. Res.,* **101,** 21 253–21 263.